




Identification of a pseudo-ternary intermetallic compound in the stirred zone of friction-stir-welded 5083 aluminum alloy with 316L steel

Mayerling Martinez Celis^{1,2,*} , Petr Harcuba², Jozef Veselý², Florent Moisy¹, Florent Picot^{1,3}, Richard Retoux¹, Bernadette Domenges¹, and Eric Hug¹

¹Laboratoire CRISMAT, ENSICAEN, CNRS, Normandie Univ, UNICAEN, 6 Boulevard du Marechal Juin, 14050 Caen Cedex 4, France

²Faculty of Mathematics and Physics, Charles University in Prague, Ke Karlovu 5, 12116 Prague 2, Czech Republic

³ACOME BP 45, Usines de Romagny, 50140 Mortain Bocage, France

Received: 15 October 2022

Accepted: 14 February 2023

Published online:

10 March 2023

© The Author(s), under exclusive licence to Springer Science+Business Media, LLC, part of Springer Nature 2023

ABSTRACT

Macrostructure, microstructure, and distribution of phases through the interface were analyzed for friction-stir-welded joints 5083 aluminum alloy and 316L steel. Several analytical techniques, including light microscopy, transmission and scanning electron microscopy, elemental analysis using X-ray spectroscopy, and electron diffraction, were used to thoroughly analyze the weld interface. The interface is characterized by a significant reduction in grain size for both aluminum alloy and stainless steel. New compounds, not corresponding to thermodynamically stable phases in the binary Al–Fe phase diagram, were found in the stirred zone (SZ) as dispersed particles. On the steel side of the welding, thin slabs of new compounds were found, as well, being interlaced with the stainless steel. The observations support that the grain refinement of stainless steel is likely due to a continuous dynamic recrystallization. The intermetallic compounds present as a layer at the interface, exhibiting nanometric grain size, were identified by electron diffraction as $\text{Al}_{13}\text{Fe}_4$ and Al_5Fe_2 phases. Concerning the intermetallic compound formed in SZ, the elemental analysis showed a compound containing principally Al and Fe, with admixture of Si and Mn. It was concluded that it is a pseudo-ternary compound with body-centered cubic structure, $Im-3$ space group, which is for the first time reported in this kind of dissimilar assembly, and is known as $\alpha\text{-Al(Fe,Mn)Si}$.

Handling Editor: P. Nash.

Address correspondence to E-mail: mayerling.martinez@ensicaen.fr

Introduction

Friction stir welding (FSW) is a solid-state joining technique invented in 1991 at the Welding Institute [1]. The principle of the welding is rather simple. A rotating tool penetrates the working piece, moves along the joint to be consolidated, and performs the welding. During the process, the material in contact with the tool and its environment undergoes plastic deformation at elevated temperatures [1]. The technique has interesting applications in aerospace, automotive, and shipbuilding industry [2]. The FSW process can be used to weld materials which are difficult to weld by means of traditional welding techniques. It is a useful technique to weld dissimilar materials in order to reduce weight of structures and combine interesting properties, for example, low density and high mechanical strength. Examples of materials which are being joined with this technique are Mg/steel [3, 4], Al/Ti [5], Al/Mg [6], Fe/Al [7, 8], and Al/Cu [9].

Numerous studies concerning FSW are focused on the characteristics of the welded region and the general performance of the piece. The studies describe residual stress measurements, microstructure characterization, mechanical properties, and corrosion behavior [4, 9–14]. It is well established that the welded region is highly affected by the process and there is an evolution of the microstructure (grain size, texture, morphology) due to the intense plastic deformation and high temperatures [1]. Other modifications of starting materials dwell in the formation of new phases during the process. When welding dissimilar materials, intermetallic compounds (IMC) can be formed. An intermetallic compound can be present as dispersed particles in the stirred material and/or at the welding interface as a continuous layer or in intercalated layers [7, 15]. Intermetallic compounds are as a rule brittle and deteriorate physical and chemical properties of materials [16]. For such reasons, the welding process parameters have to be carefully optimized in order to obtain a correct amount of intermetallic phases, which ensure the best performance of the piece.

Different studies concerning the FSW of aluminum alloys and steels have been reported in the literature [8, 17–24]. In particular, the study of the microstructure of the welding region and the type and thickness of IMC formed are useful to understand the quality of

the bonding. Bozzi et al. [25] concluded that the thickness of the IMC layer must be limited to a few μm in order to have good weld strength. In this study FeAl_3 , Fe_2Al_5 , and FeAl_2 were identified in the IMC region. Kimapong and Watanabe [26] studied changes in mechanical behavior and type of intermetallic compounds as depending on the welding parameters. They concluded that, from all Fe–Al identified compounds, FeAl_3 deteriorates mechanical properties of the joint. Lan et al. [17] reported an IMC layer which consisted of AlFe or Al_3Fe depending on the welding conditions. Springer et al. [27] and Jiang et al. [28] identified Al_5Fe_2 and $\text{Al}_{13}\text{Fe}_4$ IMC in the welding region. Huang et al. [29] and Liu et al. [30] used a spatially designed tool in order to control the intermetallic layer at the interface; in this way, they obtained a joint with less defects, thinner interfacial layer and improved mechanical properties.

The identification of IMC is generally performed by elemental analysis, while electron diffraction and X-ray diffraction are employed less frequently. If the intermetallic contains two elements (Fe and Al), identification by elemental analysis is rather straightforward, based on the Fe/Al ratio. When a third element is present together with Fe and Al, the situation can be different. The third element could be dissolved in a binary intermetallic phase, not changing the crystal structure, or it can form a ternary compound. The examination of phase diagrams of some of the Fe–Al–X systems shows the complexity of the situation. In our study, the relevant elements are, e.g., Cr, Ni, Mn, and Si, which are present in the alloys being joined. Concerning Ni, Zhang et al. [31] studied experimentally the Al–Fe–Ni system with the Al concentration above 50 at.%. It was determined that at $T = 627^\circ\text{C}$ the solubility of Ni in $\text{Al}_{13}\text{Fe}_4$, Al_5Fe_2 , and Al_2Fe is small. Once the solubility limit of Ni in these phases is exceeded, two ternary intermetallic compounds appear, namely Al_9FeNi and $\text{Al}_{10}\text{Fe}_3\text{Ni}$. On the other hand, Krendelsberger et al. [32] studied the Fe–Al–Si system and found also ternary compounds in the Al rich corner. At $T = 550^\circ\text{C}$, the hexagonal phase $\text{Al}_{7.4}\text{Fe}_2\text{Si}$ and monoclinic $\text{Al}_9\text{Fe}_2\text{Si}_2$ are stable. Experimental studies are also supported by assessment of the phase diagrams, which improve the description of ternary systems [33–35]. These are only few of many examples which show that alloying elements have to be considered carefully in order to correctly analyze new phases formed during the welding process.

Another aspect, not considered so far extensively, is the influence of the process in the lower plate during FSW in the lap or transparent configuration, which is the one employed in the present work. In this type of geometry, the two materials to be welded are superimposed, the softer material is on the top, the harder material being underneath. During the welding, the tool penetrates the upper plate entirely. In addition, the pin tool scratches the surface of lower plate. As a consequence, the alloy beneath the pin also undergoes thermomechanical treatment, while temperature and strain could be sufficient to drive changes in microstructure.

The objective of the present work is to determine modifications of the region at the interface formed during FSW of aluminum 5083 alloy and 316L stainless steel. Various microscopy techniques have been employed to characterize the interface between the welded materials on different scales. New phases have been carefully analyzed by coupling elemental analysis with electron diffraction techniques. The work demonstrates difficulties encountered at phase identification when more than two elements are present in the compounds. A special attention is on a rarely studied modification of the steel microstructure. The microstructure modifications can be associated with recrystallization processes.

Experimental

Experimental setup and materials

The welding of the aluminum alloy and the stainless steel was performed using a FSW configuration, inspired by Kimapong and Watanabe [8, 23]. The chemical analysis of the aluminum alloy and the steel used in this study, as well as the thickness of the plates, is given in Table 1.

The tool used for welding is made of tungsten carbide with a threaded probe with conical shape. The specific dimensions of the tool and the lap configuration setup are depicted in Fig. 1a. During the process, the tool (Fig. 1b) penetrates entirely the aluminum plate and scratches the surface of the steel. In the welding region, the aluminum alloy is stirred by the pin with a 3° tilt. The penetration depth inside the stainless steel is set at 0.35 mm. In a previous study [8], the authors worked with a rotation speed of the tool between 600 and 2100 rpm, and a welding

Table 1 Chemical composition of the alloys (wt%) and thickness of the plates at the welding position

Aluminum 5083 (Al balance)—plate thickness 4.85 mm							
Mg	Si	Fe	Cu	Mn	Cr	Zn	Ti
4.0–4.9	0.40	0.40	0.10	0.25	0.05–0.25	0.20	0.15
Stainless steel 316L (Fe balance)—plate thickness 3.5 mm							
C	Si	Mn	Cr	Ni	Mo	–	–
0.025	0.40	1.20	16.80	10.10	2.10	–	–

speed in the 10–100 mm·min⁻¹ range. In the present work, the parameters were chosen to have a sound weld in which the defects are minimized and the mechanical properties are optimized. For more details concerning mechanical properties and welding conditions, one can see [8].

Material characterization

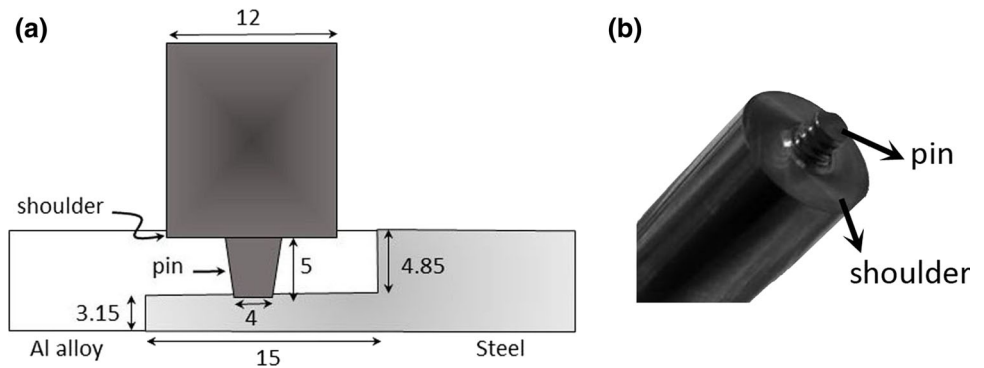
The welding region was analyzed using optical and electron microscopy methods. Two scanning electron microscopies (SEM) were used, the JEOL system coupled with BRUKER EBSD camera, and the ZEISS Auriga Compact equipped with EDAX EBSD camera and EDS detector. The study of the fine microstructure of the interface was performed using two transmission electron microscopes (TEM): a JEOL 2010 and a JEOL 2200FS, all operating at 200 kV. The samples for SEM observations were prepared by traditional mechanical polishing, the final polishing was performed using OPS suspension. Electrolytic polishing was also undertaken for selected samples by means of Struers Lectropol using A2 electrolyte. The thin foils for TEM observations were prepared in the SEM/ZEISS Auriga Compact equipped with a focused ion beam (FIB) and easy-lift manipulator designed for In-Situ Lift-Out thin lamella preparations.

Results and discussion

Microstructure changes: grain refinement of aluminum and stainless steel

Macroscopic observation of the welded region revealed a good weld quality without macroscopic

Figure 1 Schematic representation of the lap friction stir welding configuration, the dimensions are in mm (a) and image of the tool employed in the present work (b).



voids or cracks. Figure 2 captures the macrostructure of the stirred zone cross section after metallographic polishing and etching. The region is perpendicular to the tool path. One can clearly see the structure of the stirred zone, also called nugget, in the center of the image. The nugget is characterized by an onion ring structure which has been already reported for other aluminum alloys and copper [36–38]. At higher magnification (not shown here), it can be seen that some particles are present in the nugget, these small particles were pulled out by the tool pin from the steel and spread in the stirred zone. Two long asymmetric intrusions of steel inside Al are observed, as well. It has been already reported that the size of such objects depends on the depth of penetration of the tool. These defects are known as hooks and/or cold lap defects.

Several EBSD analyses were performed in the nugget region; the one shown in Fig. 3 is located near the Al/steel interface (highlighted in yellow in Fig. 2). The structure of aluminum corresponds to a very fine-grain microstructure of equiaxial grains. The average grain size in the stirred zone is 5.6 μm , which is at least one order of magnitude smaller than the grain size in the starting material ($\approx 80 \mu\text{m}$). There is a spatial distribution of the average grain size, which depends on the distance to the aluminum/steel interface. This observation is in agreement with previous studies and is related to the variations of temperature in the stirred zone [1, 39]. The temperature is higher in the region in contact with the pin shoulder, and the corresponding grain size is slightly larger in this region. The abrupt decrease in grain size of Al in the nugget region, when comparing to the starting metal, can be generally attributed to a dynamic recrystallization operating during the welding process [1, 39]. TEM images near the interface of the welding show that the

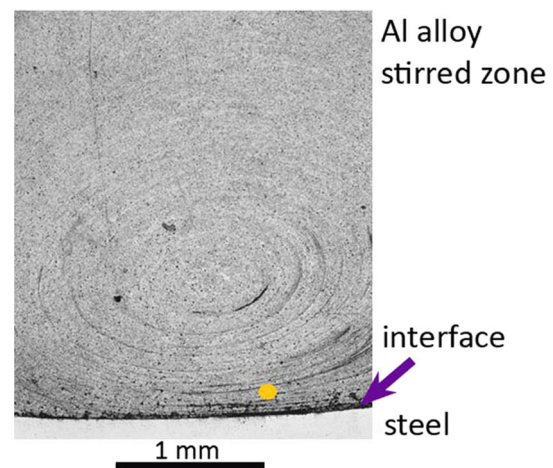


Figure 2 Macrostructure of the welded region after etching with Keller's etchant (1.5% HCl, 2.5% HNO_3 , 0.5% HF and 95.5% H_2O).

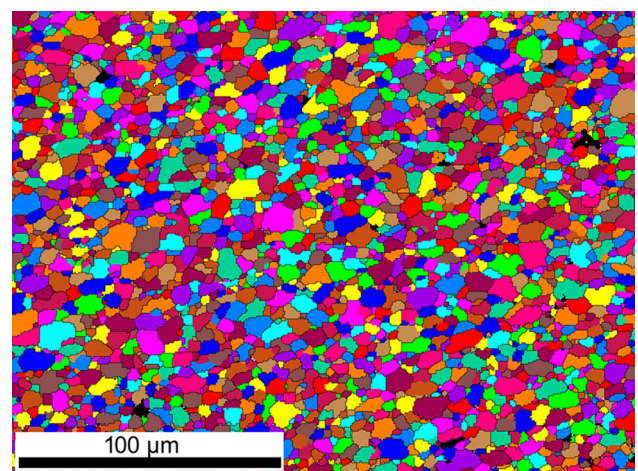


Figure 3 Map of grains in the aluminum nugget zone as determined by SEM/EBSD.

aluminum grains are smaller in this region and contain low density of dislocations (Fig. 7). This fact may be related to an incomplete recovery in this region [40, 41].

The changes in the microstructure in the stirred zone are in agreement with other analyses for Al alloys [27, 39, 42, 43].

The microstructure of the stainless steel is affected by the FSW process, as well, as seen in Fig. 4. The impact on the steel microstructure depends on the distance from the interface. The changes are progressive and depend on the intensity of the thermo-mechanical process, which increases when approaching the aluminum/steel interface. Far away from the interface, at around 450 μm (Fig. 4a), its intensity is low. In this region the grains are deformed, as manifested by a spread in orientation inside the grains, visible by color variations. When

approaching the interface, at about 300 μm , the grains are more and more elongated and have a higher spread in orientation, while the deformation of the grains roughly follows the sense of rotation of the tool. In some regions, microdeformation bands are developed over the original grains, and there are also some high-angle grain boundaries which develop inside grains and finish inside them, see Fig. 4b (black arrows). In some grains the deformation bands are progressively subdivided, with the formation of new and smaller crystals, Fig. 4b (white arrows). The formation of new smaller grains occurs both in grains interiors and at high-angle boundaries. At around 30 μm from the interface, the grains are highly elongated, with a mean transverse grain size which can be as small as 0.6 μm , and aspect ratio as high as 6.5. Finally, near the interface, where the temperature and mechanical loading are the highest, sub-micrometer

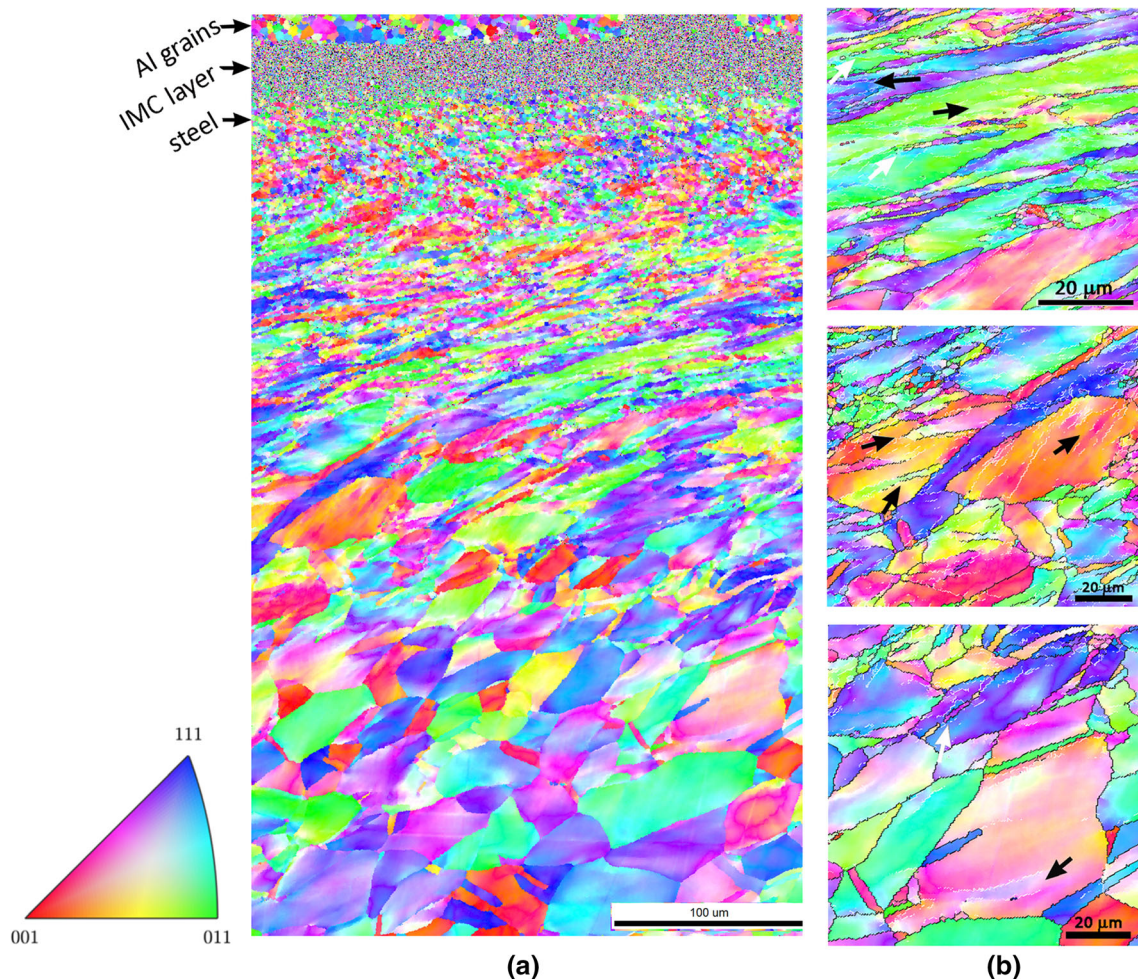


Figure 4 EBSD map of the microstructure of 316L near the interface: General view (a), detail of the microstructure at 300 μm from the interface (b). HAGB ($> 15^\circ$) are depicted in black, LAGB ($< 15^\circ$) in white.

grains with mixed morphology occur. Some of them are equiaxial (with a grain size of ≈ 100 nm), others elongated (aspect ratio ≈ 3), but always exhibit a high dislocation density irrespective of their shape (Fig. 5).

The process induces a very strong grain refinement, near the interface/close to the pin tool path, as the grain size of steel is more than two orders of magnitude smaller than the one of original stainless steel ≈ 45 μm . The refinement occurring under plastic deformation is frequently attributed to dynamic recrystallization (DRX). Whether a material undergoes continuous DRX (CDRX) or discontinuous DRX (DDRX) depends on several factors: the stacking fault energy of the material, the imposed strain, or the temperature of the process [44–46].

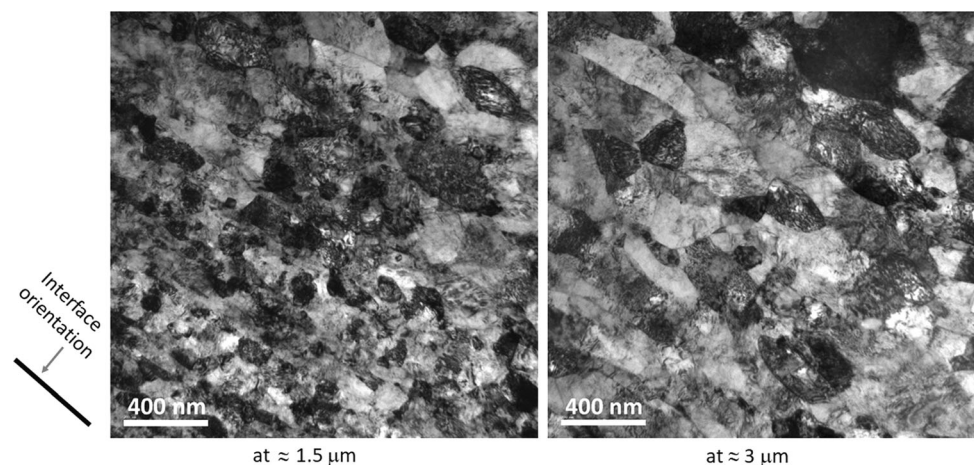
Austenitic stainless steel is considered as an alloy with medium to low stacking fault energy (SFE). It has been reported that the SFE is about 64 mJ/m^2 [47]. The rather low SFE permits the formation of stacking faults, and in such conditions cross-slip or climb during deformation is rather difficult. As a consequence, the re-arrangement of dislocations is more difficult and defects tend to accumulate inside the grains.

Concerning temperature measurements in the vicinity of the stirred region, they are very difficult because of the intense plastic deformation produced by the movement of the tool. The temperatures within and nearby the stirred zone have been estimated by examination of the microstructure of the welded region, or measured by embedding thermocouples in the tool or in the workpiece [1, 48]. In the present work none of these methods were employed, but we can reasonably suppose that the maximum

temperature is below the melting point of Al alloy, since FSW is a solid state process and the characteristic of the welding region are those of a solid state welding. Considering the maximum temperature achieved in the nugget below 600 $^{\circ}\text{C}$, the temperature in the 316L steel could be also reasonably estimated not to exceed 600 $^{\circ}\text{C}$. The measurement of temperature in a study of the welding of Al/Ti performed using similar process parameters support this assumption. During the welding of this couple, one thermocouple was placed inside Ti, at 3 mm beneath the Al/Ti initial interface. The results indicated that the temperature peak occurs between 410 and 450 $^{\circ}\text{C}$ in Ti. This result could be extrapolated to our work, as titanium has a similar thermal conductivity as 316L steel. Consequently, we can suppose quite comfortably that the temperature in steel is lower than half its melting point T_m .

Taking into account these two factors, we can examine the features of DRX to understand the type of refinement that the steel underwent. On the one hand, DDRX is a recrystallization phenomenon which usually occurs during hot deformation of alloys with low to medium SFE [45, 49]. Furthermore, the mechanism involves serration of the initial grain boundaries, local bulging of this boundaries, and grow of the new grains by consumption of the defected surroundings. New grains nucleate at grain boundaries, a necklace structure may form in some cases. On the other hand, CDRX occurs in all metallic materials at $T < 0.5 T_m$ and in materials with medium to high SFE also at $T > 0.5 T_m$ [43, 47]. During the deformation, there is formation of low angle boundaries, and a gradual evolution into high angle grain boundaries (HAGB). The new grains are

Figure 5 TEM image of the steel microstructure beneath the pin tool at different distances from the interface.



formed as a result of the gradual rotation of grains with the work hardening, there is an accumulation of dislocations at the boundaries, which produces a continuous increase of misorientation across the deformation induced boundaries, until the gradual transformation to HAGB [44, 50].

The temperature beneath the pin tool during the FSW of Al and steel, as explained before, is estimated to be lower than $0.5 T_m$ of the steel, and this material has a rather low to medium SFE. These two parameters are characteristics of continuous DRX process, which is probably the mechanism responsible for the refinement of the steel in the region near the interface.

The examination of the microstructure corroborates this hypothesis. There is neither evidence of grain boundary bulging nor necklace formation characteristic of DDRX. Features indicative of CDRX are the presence of microbands, portions of boundaries of high angle misorientation finishing inside the grains, high density of dislocations in the new recrystallized grains, and the formation of recrystallized grains in grain interiors, all these features were observed in our samples. This type of DRX has been already observed in other stainless steels [48–52], as well as in the Ni-20Cr alloy [53]. These alloys have similar medium to low SFE, and the CDRX phenomena were observed at temperatures below $0.5 T_m$.

Identification of intermetallic compounds

Microstructure and phases through the interface were studied by elemental analysis and electron diffraction set ups using both SEM and TEM. Figure 6 shows a global view of the interface after the welding using backscattered electrons. One can observe on the steel side of the weld (light grey) the presence of intercalated layers of different phases which are distinguished by different contrast and composition (black arrows). Individual layers correspond to the steel itself (light grey) and to a compound formed by diffusion of elements during the thermomechanical welding (grey). One can also distinguish in the stirred zone a dispersion of particles in the aluminum matrix (white arrows). The pin tool stripped off steel particles from the interphase during the welding and spread it in the nugget. In parallel, diffusion occurs changing the composition and hence the phase of the particles. The putative new phases (both the layers and the particles) formed by the FSW process were analyzed by EDS.

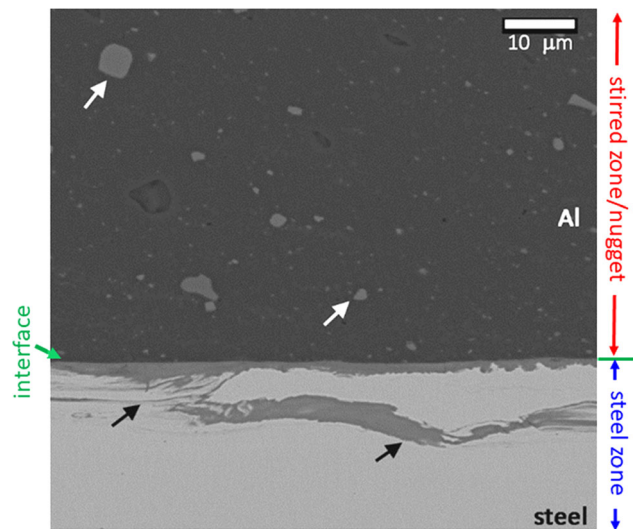


Figure 6 SEM image, in chemical contrast, near the interface of the welded region. Steel appears in light grey (bottom part of image), aluminum nugget in dark grey (upper part of the image) and intermetallic compounds in grey. The interface is highlighted in green. The white arrows indicate the intermetallic particles dispersed in the nugget, and the black arrows indicate the intermixed layer of intermetallic compounds.

Concerning the nugget, around 20 particles of different sizes ($2\text{--}8\ \mu\text{m}$) from the vicinity of the interface were chosen for analysis. The results show that they are rich in Al but contain also Fe, Mn, Si, a low quantity of Cr, and in some cases a low quantity of Mg (Table 2). The presence of elements as Mn or Si has to be considered carefully in order to correctly identify the new compound formed during the welding. The deduction of the nature of the phase formed cannot be directly established from the calculation of the Al/Fe ratio.

Several experimental studies and thermodynamic assessments agree that in the Al rich corner of the Al–Fe–Mn–Si system there are three ternary phases and one pseudo-ternary phase [54–56]. The crystal structure of the pseudo-ternary Al(Fe,Mn)Si is cubic. It can appear, depending on the composition, as having a simple cubic or body-centered cubic structure. In order to explore these options, 13 of these particles were analyzed by EBSD. Despite good quality of the electron backscatter diffraction patterns (EBSP), the discrimination between the crystal structures was not possible. The careful analysis of the EBSP adding more Kikuchi lines, to consider some bands which have a weak contrast, in order to better assess the

Table 2 Elemental composition range (in at.%) of the IMC particles embedded in the Al matrix. The Mn to Fe ratio is also reported

	Al	Si	Cr	Mn	Mg	Fe	Mn/Fe
IMC particles embedded in the Al matrix, in the nugget	77.0–79.6	4.4–5.5	0.4–1.1	4.4–6.0	0–1.6	8.6–11.1	0.5–0.6

differences between the space groups, was not successful.

The Mn/Fe ratio is a variable which seems to be crucial in the transition between the simple cubic structure with the $Pm-3$ space group and the body-centered cubic one with the $Im-3$ space group. In another words, changes of the Mn/Fe ratio drive an order–disorder transition. The phase has a simple cubic structure with $Pm-3$ space group, which changes to the body-centered cubic with $Im-3$ space group with increasing Fe concentration, i.e., decreasing the Mn/Fe ratio [56–58]. The ratio at which the transition occurs has been studied by several authors [57–59]. They all concluded that a low Mn/Fe ratio favors the body-centered cubic structure while the high ratio favors the simple cubic one. Donnadiou et al. [58] reported the ratio between 1 and 3, Yoo et al. [57] concluded that the ratio depends on heat treatment and that the transition occurs at 1.6, while the critical value for Kim et al. [59] lies between 0.11 and 0.66. It is interesting to point out here that these studies were performed for Al alloys and that the phases are particles which precipitate due to the presence of alloying elements.

The above explanation seems to indicate that the IMC could have a cubic structure with $Im-3$ space group, as the Mn/Fe ratio in the analyzed particles is very low, between 0.5 and 0.6 (Table 2). In order to investigate more precisely these intermetallic compounds and to discriminate between the two possible structures, TEM observations were performed in a region containing an intermetallic particle dispersed in the stirred zone as well as in the region with intercalated layers of different phases (Fig. 6). A global view of the region studied is presented in Fig. 7. The region corresponding to the stirred zone is highlighted in red, the region corresponding to steel in blue. In the stirred zone, we can observe an intermetallic particle, while in the steel region the intercalated layers can be distinguished by different grey contrast. A closer view of the region evidences that the intermetallic layer consists of nanocrystals.

Several electron diffraction patterns were analyzed in order to identify the crystal structure of the particle. The electron diffraction patterns along the [111] and [113] zone axes are presented in Fig. 8a and b, respectively. The diffraction patterns for the $Im-3$ and $Pm-3$ space groups, simulated using the JEMS software [60], are shown for comparison. The simulated patterns are practically identical for these two orientations; hence, it is impossible to conclude about the correct space group. In order to distinguish between these space groups, the crystal must be oriented in a specific direction so as to highlight the differences in extinction conditions for each structure. Figure 9 shows the [112] axis of the same particle and the corresponding JEMS simulation for the two different space groups. The simulated pattern shows that there is a crucial difference in this case. While all reflections are permitted for the $Pm-3$ space group, for the $Im-3$ space group the reflections for which $h + k + l$ is odd do not appear. From this it can be concluded that the phase observed is cubic with the $Im-3$ space group and the unit cell parameter of about 12.6 Å. All particles analyzed using EDS in SEM are in the same range of composition as the one analyzed in TEM. More significant, the Mn/Fe ratio of all particles, which is an important parameter in the determination of the phase is very low, not higher than 0.6. Taken into account these two facts, we conclude that the particles at the interface with similar composition correspond to α -Al(Fe,Mn)Si, as the one analyzed in TEM, with cubic structure and $Im-3$ space group.

On the other hand, the region with intercalated layers also represents a new compound, but the composition is slightly different from the particles. Namely, the concentration of aluminum is higher, while the Mn concentration is much lower, and no Mg was detected in this region (Table 3).

The layers containing intermetallic compounds with grains of nanometer size were also studied using TEM. The grains of IMC in the outer layer, in contact with the Al alloy, are equiaxial, while those in contact with the steel (inner layer) are more

Figure 7 TEM image showing the global view of the microstructure at the interface of the welding. The nugget contains small Al grains and one intermetallic particle (in the lower/right part of the image). The steel side of the welding in which the layers of intermetallic are intermixed is located at the upper/right part of the image. The interface is marked by green arrows.

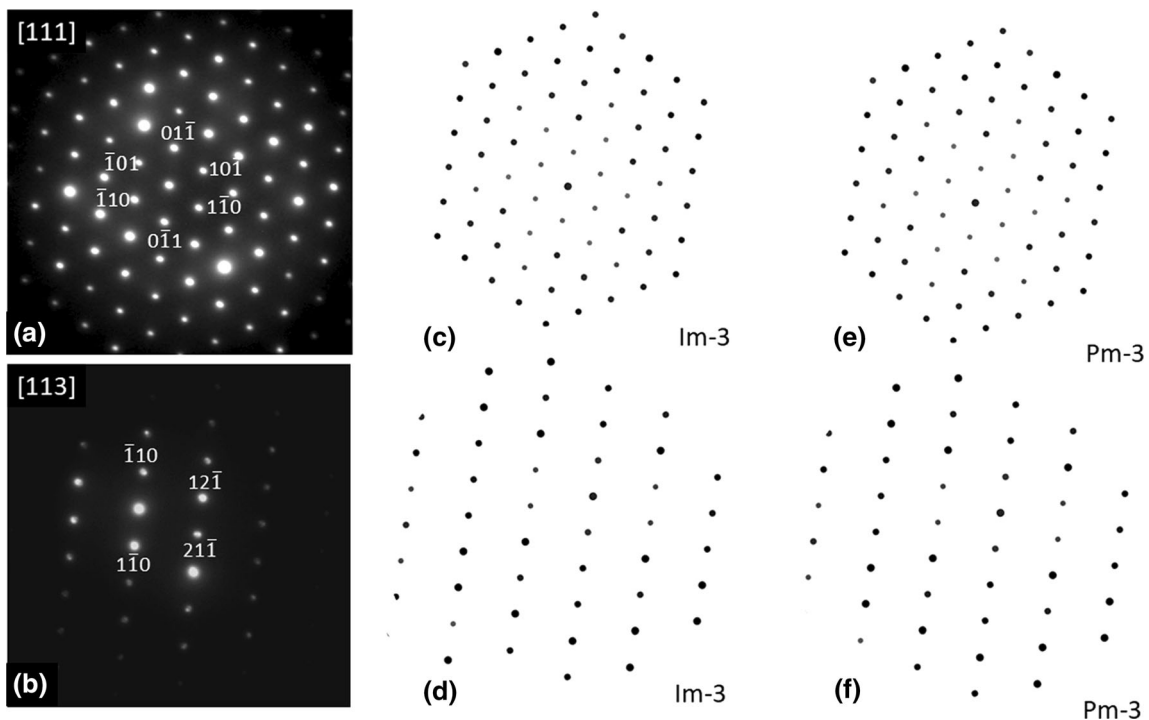
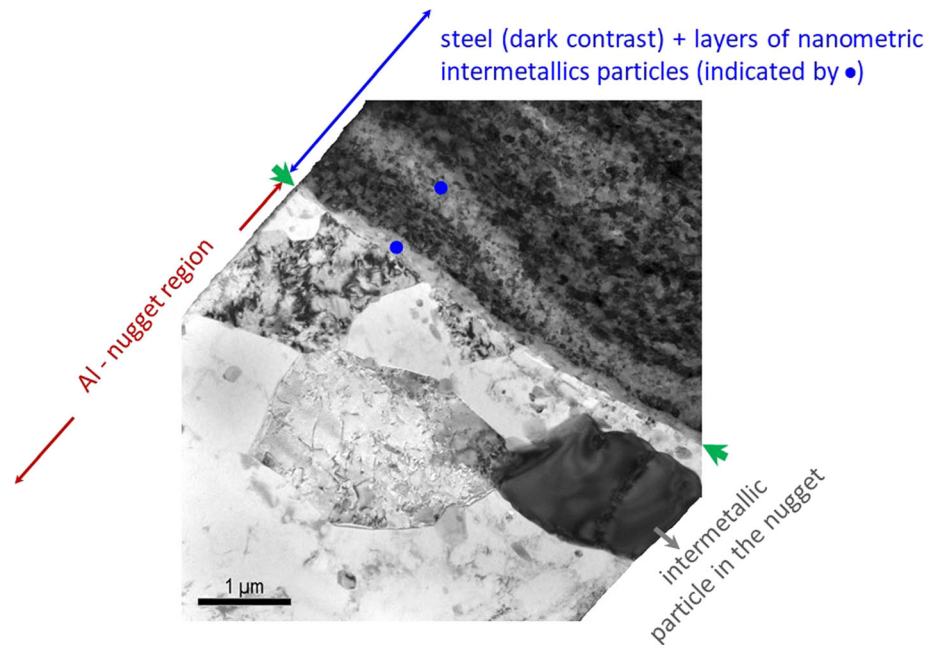


Figure 8 Experimental selected area diffraction patterns (SADP) of an IMC particle located near the interface for the [111] (a) and [113] (b) zone axes, and simulated patterns at the same orientations for *Im-3* (c), (d) and *Pm-3* (e), (f) space groups.

columnar, as can be observed in Fig. 10a. The elemental mapping in Fig. 10b shows the distribution of Al, Mg, Fe, and Cr in a region near the interface. Here, steel is at the bottom, the intermetallic layer in the middle, and the Al alloy at the top of each scan. Al is located, as expected, in the IMC layer and the

nugget, while Mg is concentrated inside the nugget. The distribution of Mg allows us to identify the nugget/IMC interface, which is visible also on the Fe map (black arrow). Fe and Cr are principally present in the steel. Using these two mappings as well as the map of Al, one can easily locate the steel/IMC

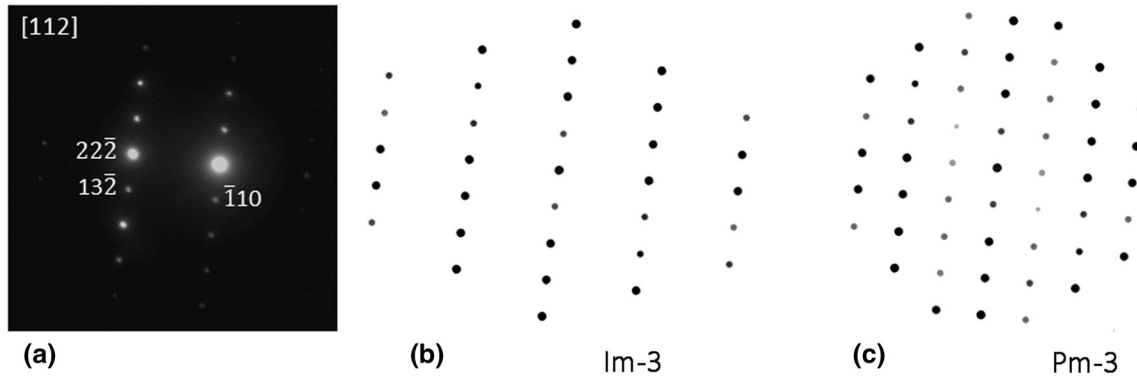


Figure 9 SADP of one IMC particle, view along the $[112]$ zone axis (a). Corresponding patterns simulated using the JEMS software for $Im-3$ (b) and $Pm-3$ (c) space groups.

Table 3 Elemental analysis of the layer between Al and 316L

	Al	Si	Cr	Mn	Fe
Layer of IMC nanoparticles	88.1–89.4	3.3–5.1	2.3	0.3	3.8–3.9

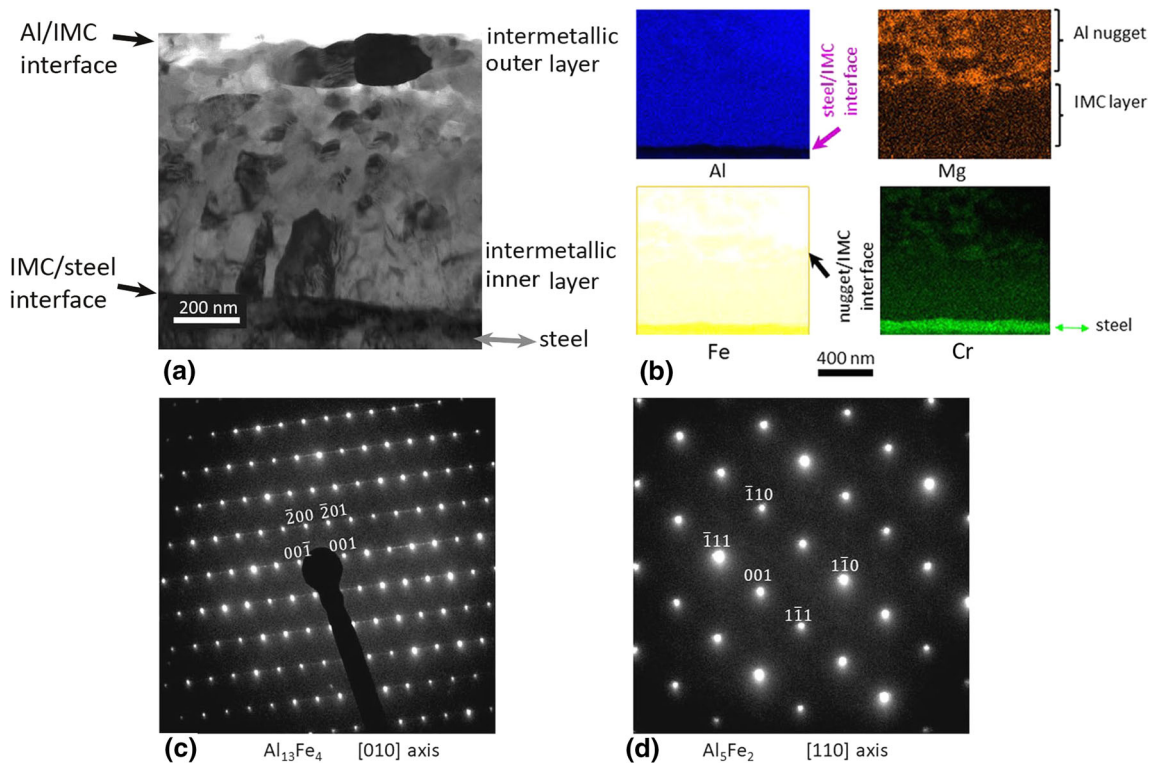


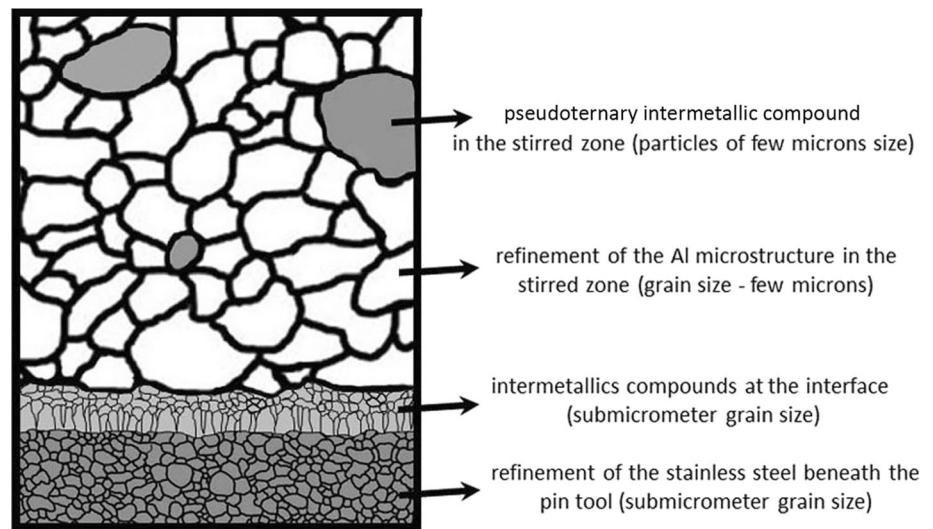
Figure 10 TEM study of the new compounds formed in the steel side of the joint (at the interface, intermixed layer): image of the intermetallic layer with nanometric grains (a), EDS map of some

representative elements near the interface (b) identification of the phases in the IMC layer: outer layer (c) and inner layer (d).

interface, which is very sharp (violet arrow). The distribution of elements in the intermetallic layer is uniform; no clear difference between the inner and

outer layer of IMC was identified using the elemental maps.

Figure 11 Schematic representation of principal features of the interface.



Several electron diffraction patterns were collected from the IMC layer, and as the grain size is nanometric, the diffraction patterns almost always contain reflections from several grains. The evaluation of several diffraction patterns indicated that the outer phase corresponds to $\text{Al}_{13}\text{Fe}_4$ with a monoclinic structure and space group $C2/m$. In Fig. 10c, which depicts the [010] zone axis of this phase, we can observe some streaks possibly related to the presence of planar defects, as already reported by Tsuchimori et al. [61] and Krivska et al. [62]. The planar defects are lying on (100), (20-1), and (001) planes, and the twinning planes have been reported as (100), (20-1), and (001). Some of these structures were observed by high resolution TEM in [61]. The presence of nanotwins in the $\text{Al}_{13}\text{Fe}_4$ phase has been also recently observed by Xu et al. [63]. Concerning the phase close to the steel, it was identified as Al_5Fe_2 with orthorhombic structure and space group $Cmcm$ (Fig. 10d).

These two phases, unlike the pseudo-ternary phase, have been already observed during FSW of aluminum alloys and steels by using various methods, namely EDS, XRD, and TEM [25, 28, 42, 64–66].

By using various electron microscopy techniques addressing different scales, we assessed the structural changes of the welded region, giving description of the microstructure of the two base alloys and the formation of new phases in different locations. Figure 11 yields a schematic summary of the present results showing all the microstructural features revealed in this work.

Conclusion

The interface of the FSW of dissimilar Al alloy and 316L steel has been investigated by electron microscopy and orientation imaging. The results reveal details of dramatic material modifications present on different length scales. The main results, concerning the grain refinement of the initial microstructure and the formation of new intermetallic phases, can be summarized as follows.

- The region in the stirred region is refined after welding, the grain size is reduced by more than one order of magnitude, and the final average grain size is about 5–6 μm .
- The microstructure of the 316L steel beneath the initial interface is also refined, and the reduction in grain size is more dramatic than in the stirred zone. The grain size is reduced by at least two orders of magnitude with respect to the base metal, with grain sizes on the submicrometric scale. The refinement is attributed to a continuous dynamic recrystallization.

The intermetallic compounds present as a layer, with grain of submicron size, were identified as the monoclinic $\text{Al}_{13}\text{Fe}_4$ phase and the orthorhombic Al_5Fe_2 phase. On the other hand, the type of IMC, present as particles in the stirred region, indicated the formation of a pseudo-ternary phase $\alpha\text{-Al}(\text{Fe},\text{Mn})\text{Si}$ (a cubic phase with the $Im\bar{3}$ space group), which is for the first time reported in this kind of dissimilar welding.

Acknowledgements

The work is part of the research project “Nanomaterials centre for advanced applications” no. CZ.02.1.01/0.0/0.0/15_003/0000485, financed by ERDF. The authors thank PROBENT (former SOMI-NEX) for providing the welded samples.

Data availability

The data that support the findings of this study are available from the corresponding author upon reasonable request.

Declarations

Conflict of interest The authors declare no conflict of interest.

Ethical approval There were not experiments concerning human tissue or similar in this article.

References

- [1] Mishra RS, Ma ZY (2005) Friction stir welding and processing. *Mater Sci Eng R* 50:1–78
- [2] Thomas WD, Nicholas ED (1997) Friction stir welding for the transportation industries. *Mater Des* 18:269–273
- [3] Jana S, Hovanski Y, Grant GJ (2010) Friction stir lap welding of magnesium alloy to steel: a preliminary investigation. *Metall Mater Trans A* 4:3173–3182
- [4] Kasai H, Morisada Y, Fujii H (2015) Dissimilar FSW of immiscible materials: steel/magnesium. *Mater Sci Eng A* 624:250–255
- [5] Wei Y, Li J, Xiong J, Huang F, Zhang F, Hamid Raza S (2012) Joining aluminum to titanium alloy by friction stir lap welding with cutting pin. *Mater Charac* 71:1–5
- [6] Shi H, Chen K, Liang Z, Dong F, Yu T, Dong X, Zhang L, Shan A (2017) Intermetallic compounds in the banded structure and their effect on mechanical properties of Al/Mg dissimilar friction stir welding joints. *J Mater Sci Technol* 33:359–366
- [7] Tanaka T, Nezu M, Uchida S, Hirata T (2020) Mechanism of intermetallic compound formation during the dissimilar friction stir welding of aluminum and steel. *J Mater Sci* 55:3064–3072. <https://doi.org/10.1007/s10853-019-04106-2>
- [8] Picot F, Gueydan A, Martinez M, Moisy F, Hug E (2018) A correlation between the ultimate shear stress and the thickness affected by intermetallic compounds in friction stir welding of dissimilar aluminum alloy-stainless steel joints. *Metals* 8:1–11
- [9] Carlone P, Astarita A, Palazzo GS, Paradiso V, Squillace A (2015) Microstructural aspects in Al–Cu dissimilar joining by FSW. *Int J Adv Manuf Technol* 79:1109–1116
- [10] Su JQ, Nelson TW, Sterling CJ (2005) Microstructure evolution during FSW/FSP of high strength aluminum alloys. *Mater Sci Eng A* 405:277–286
- [11] Staron P, Ko M, Williams S, Wescott A (2004) Residual stress in friction stir-welded Al sheets. *Physica B* 350:e491–e493
- [12] De Giorigi M, Scialpi A, Panella FW, De Filippis LAC (2009) Effect of shoulder geometry on residual stress and fatigue properties of AA6082 FSW joints. *J Mech Sci Technol* 23:26–35
- [13] Corral J, Trillo EA, Li Y, Murr LE (2000) Corrosion of friction-stir welded aluminum alloys 2024 and 2195. *J Mater Sci Lett* 19:2117–2122
- [14] Atapour M, Pilchak A, Frankel GS, Williams JC (2010) Corrosion behaviour of investment cast and friction stir processed Ti–6Al–4V. *Corros Sci* 52:3062–3069
- [15] Safeen MW, Spina PR (2019) Main issues in quality of friction stir welding joints of aluminum alloy and steel sheets. *Metals* 9:1–22
- [16] Moisy F, Gueydan A, Sauvage X, Guillet A, Keller C, Guilmeau E, Hug E (2018) Influence of intermetallic compounds on the electrical resistivity of architected copper clad aluminum composites elaborated by a restacking drawing method. *Mater Des* 155:366–374
- [17] Lan S, Liu X, Ni J (2016) Microstructural evolution during friction stir welding of dissimilar aluminum alloy to advanced high-strength steel. *Int J Adv Manuf Technol* 82:2183–2193
- [18] Yazdipour A, Heidarzadeh A (2016) Effect of friction stir welding on microstructure and mechanical properties of dissimilar Al 5083–H321 and 316L stainless steel alloys joints. *J Alloys Compd* 680:595–603
- [19] Yazdipour A, Heidarzadeh A (2016) Dissimilar butt friction stir welding of al 5083–H321 and 316L stainless steel alloys. *Int J Adv Manuf Technol* 87:3105–3112
- [20] Chen T (2009) Process parameters study on FSW joint of dissimilar metals for aluminum-steel. *J Mater Sci* 44:2573–2580. <https://doi.org/10.1007/s10853-009-3336-8>
- [21] Elrefaey A, Gouda M, Takahashi M, Ikeuchi K (2005) Characterization of aluminum/steel lap joint by friction stir welding. *J Mater Eng Perform* 14:10–17
- [22] Nishida T, Ogura T, Nishida H, Fujimoto M, Takahashi M, Hirose A (2014) Formation of interfacial microstructure in a friction stir welded lap joint between aluminium alloy and stainless steel. *Sci Technol Weld Join* 19:609–616

- [23] Kimapong K, Watanabe T (2004) Friction stir welding of aluminum alloy to steel. *Weld J* 83:277–282
- [24] Derazkola HA, Aval HJ, Elyasi M (2015) Analysis of process parameters effects on dissimilar friction stir welding of AA1100 and A441 AISI steel. *Sci Technol Weld Join* 20:553–562
- [25] Bozzi S, Helbert-Etter AL, Baudin T, Criqui B, Kerbiguet JG (2010) Intermetallic compounds in Al 6016/IF-steel friction stir spot welds. *Mater Sci Eng A* 527:4505–4509
- [26] Kimapong K, Watanabe T (2005) Lap joint of A5083 aluminum alloy and SS400 steel by friction stir welding. *Mater Trans* 46:835–841
- [27] Springer H, Kostka A, Dos Santos JF, Raabe D (2011) Influence of intermetallic phases and Kirkendall-porosity on the mechanical properties of joints between steel and aluminium alloys. *Mater Sci Eng A* 528:4630–4642
- [28] Jiang WH, Kovacevic R (2004) Feasibility study of friction stir welding of 6061–T6 aluminium alloy with AISI 1018 steel. *Proc Inst Mech Eng Part B J Eng Manuf* 218:1323–1331
- [29] Huang Y, Wan L, Si X, Huang T, Meng X, Xie Y (2019) Achieving high-quality Al/steel joint with ultrastrong interface. *Metal Mater Trans A* 50:295–299
- [30] Liu J, Hao Z, Xie Y, Meng X, Huang Y, Wan L (2022) Interface stability and fracture mechanism of Al/Steel friction stir lap joints by novel designed tool. *J Mater Process Tech* 300:117425
- [31] Zhang L, Du Y, Xu H, Tang C, Chen H, Zhang W (2008) Phase equilibria of the Al–Fe–Ni system at 850 °C and 627 °C. *J Alloys Compd* 454:129–135
- [32] Krendelsberger N, Weitzer F, Schuster JC (2007) On the reaction scheme and liquidus surface in the ternary system Al–Fe–Si. *Metal Mater Trans A* 38:1681
- [33] Liu ZK, Chang YA (1999) Thermodynamic assessment of the Al–Fe–Si system. *Metal Mater Trans A* 38:1081–1095
- [34] Eleno L, Vezelý L, Sundman B, Cieslar M, Lacaze J (2010) Assessment of the Al corner of the ternary Al–Fe–Si system. *Mater Sci Forum* 649:523–528
- [35] Eleno L, Frisk K, Schneider A (2006) Assessment of the Al–Fe–Si system. *Intermetallics* 14:1276–1290
- [36] Alvarez P, Janeiro G, Da Silva AAM, Aldanondo E, Echeverría A (2010) Material flow and mixing patterns during dissimilar FSW. *Sci Technol Weld Join* 15:648–665
- [37] Krishnan KN (2002) On the formation of onion rings in friction stir welds. *Mater Sci Eng A* 327:246–251
- [38] Teimournezhad J, Masoumi A (2010) Experimental investigation of onion ring structure formation in friction stir butt welds of copper plates produced by non-threaded tool pin. *Sci Technol Weld Join* 15:166–170
- [39] Li Y, Murr LE, McClure JC (1999) Flow visualization and residual microstructures associated with the friction-stir welding of 2024 aluminum to 6061 aluminum. *Mater Sci Eng A* 271:213–223
- [40] Jata KV, Semiatin SL (2000) Continuous dynamic recrystallization during friction stir welding of high strength aluminium alloy. *Scripta Mater* 43:743–749
- [41] Su JQ, Nelson TW, Mishra R, Mahoney M (2003) Microstructural investigation of friction stir welded 7050–T651 aluminium. *Acta Mater* 51:713–729
- [42] Coelho RS, Kostka A, Dos Santos JF, Kaysser-Pyzalla A (2012) Friction-stir dissimilar welding of aluminium alloy to high strength steels: mechanical properties and their relation to microstructure. *Mater Sci Eng A* 556:175–183
- [43] Uzun H, Dalle Donne C, Argagnotto A, Ghidini T, Gambaro C (2005) Friction stir welding of dissimilar Al 6013–T4 To X₅CrNi₁₈₋₁₀ stainless steel. *Mater Des* 26:41–46
- [44] Satheesh Kumar SS, Vasanth M, Singh V, Ghosal P, Raghu T (2017) An investigation of microstructural evolution in 304L austenitic stainless steel warm deformed by cyclic channel die compression. *J Alloys Compd* 699:1036–1048
- [45] Huang K, Logé RE (2016) A review of dynamic recrystallization phenomena in metallic materials. *Mater Des* 111:548–574
- [46] Humphreys FJ, Hatherly M (2004) Recrystallization and related annealing phenomena. Elsevier, UK
- [47] Hajian M, Abdollah-zadeh A, Rezaei-Nejad SS, Assadi H, Hadavi SMM, Chung K, Shokouhimehr M (2015) Microstructure and mechanical properties of friction stir processed AISI 316L stainless steel. *Mater Des* 67:82–94
- [48] Silva ACF, De Backer J, Bolmsjö G (2017) Temperature measurements during friction stir welding. *Int J Adv Manuf Technol* 88:899–2908
- [49] Heidarzadeh A, Mironov S, Kaibyshev R, Çam G, Simar A, Gerlich A, Khodabakhshi F, Mostafaei A, Field DP, Robson JD, Deschamps A, Withers PJ (2021) Friction stir welding/processing of metals and alloys: a comprehensive review on microstructural evolution. *Prog Mater Sci* 117:100752
- [50] Tikhonova M, Belyakov A, Kaibyshev R (2013) Strain-induced grain evolution in an austenitic stainless steel under warm multiple forging. *Mater Sci Eng A* 564:413–422
- [51] Yanushkevich Z, Dobatki SV, Belyakov A, Kaibyshev R (2017) Hall-Petch relationship for austenitic stainless steels processed by large strain warm rolling. *Acta Mater* 136:39–48
- [52] Yanushkevich Z, Lugovskaya A, Belyakov A, Kaibyshev R (2016) Deformation microstructures and tensile properties of an austenitic stainless steel subjected to multiple warm rolling. *Mater Sci Eng A* 667:279–285

- [53] Dudova N, Belyakov A, Sakai T, Kaibyshev R (2010) Dynamic recrystallization mechanisms operating in a Ni–20%Cr alloy under hot-to-warm working. *Acta Mater* 58:3624–3632
- [54] Balitchev E, Jantzen T, Hurtado I, Neuschütz D (2003) Thermodynamic assessment of the quaternary system Al–Fe–Mn–Si in the Al-rich corner. *Comput Coupling Phase Diagr Thermochem* 27:275–278
- [55] Davignon G, Serneels A, Verlinden B, Delaey L (1996) An isothermal section at 550 °C in the Al-rich corner of the Al–Fe–Mn–Si system. *Metal Mater Trans A* 27:3357–3361
- [56] Lacaze J, Eleno L, Sundman B (2010) Thermodynamic assessment of the aluminum corner of the Al–Fe–Mn–Si system. *Metal Mater Trans A* 41:2208–2215
- [57] Yoo JE, Shan A, Moom IG, Maeng SJ (1999) A study on composition and crystal structure of dispersoids in AlMgSi alloys. *J Mater Sci* 34:2679–2683. <https://doi.org/10.1023/A:1004673321013>
- [58] Donnadiou P, Lapasset G, Sanders TH (1994) Manganese-induced ordering in the α -(Al–Mn–Fe–Si) approximant phase. *Philos Mag Lett* 70:319–326
- [59] Kim HY, Park TY, Han SW, Lee HM (2006) Effects of Mn on the crystal structure of α -Al(Mn, Fe)Si particles in A356 alloys. *J Cryst Growth* 291:207–211
- [60] Stadelmann PA (1987) EMS—a software package for electron diffraction analysis and HREM image simulation in materials science. *Ultramicroscopy* 21:131–145
- [61] Tsuchimori M, Ishimasa T, Fukano Y (1992) Crystal structures of small Al-rich Fe alloy particles formed by a gas-evaporation technique. *Philos Mag B* 66:89–108
- [62] Křivská B, Šlapáková M, Veselý J, Kihoulou M, Fekete K, Minárik P, Králík R, Grydin O, Stolbchenko M, Schaper M (2021) Intermetallic phases identification and diffusion simulation in twin-roll cast Al–Fe clad sheet. *Materials* 14:7771
- [63] Xu P, Hua X, Shen C, Mou G, Li F (2021) Formation of Fe₅Si₃ precipitate in the Fe₂Al₅ intermetallic layer of the Al/steel dissimilar arc welding joint: a transmission electron microscopy (TEM) study. *Mater Charact* 178:111236
- [64] Movahedi M, Kokabi AH, Seyed Reihhani SM, Najafi H (2011) Mechanical and microstructural characterization of Al-5083/St-12 lap joints made by friction stir welding. *Proc Eng* 10:3297–3303
- [65] Chen ZW, Yazdani S, Littlefair G (2013) Effects of tool positioning on joint interface microstructure and fracture strength of friction stir lap Al-to-steel welds. *J Mater Sci* 48:2624–2634. <https://doi.org/10.1007/s10853-012-7056-0>
- [66] Das H, Ghosh RN, Pal TK (2014) Study on the formation and characterization of the intermetallics in friction stir welding of aluminum alloy to coated steel sheet lap joint. *Metall and Mater Trans A* 45:5098–5106

Publisher's Note Springer Nature remains neutral with regard to jurisdictional claims in published maps and institutional affiliations.

Springer Nature or its licensor (e.g. a society or other partner) holds exclusive rights to this article under a publishing agreement with the author(s) or other rightsholder(s); author self-archiving of the accepted manuscript version of this article is solely governed by the terms of such publishing agreement and applicable law.